Landé *g* factors in tetragonal halide perovskite: A multiband k.p model

G. Garcia-Arellano,[1] K. Boujdaria,[2,*] M. Chamarro,[1] and C. Testelin[1]
[1]*Sorbonne Université, CNRS, Institut des NanoSciences de Paris, F-75005, Paris, France*
[2]*Université de Carthage, Faculté des Sciences de Bizerte, LR01ES15 Laboratoire de Physique des Matériaux: Structure et Propriétés, 7021 Zarzouna, Bizerte, Tunisia*

(Received 8 July 2022; revised 13 September 2022; accepted 14 September 2022; published 3 October 2022)

In the framework of **k.p** theory, we have calculated the expressions for *g* factors for electrons and holes taking into account up to 16-band contributions for materials with tetragonal symmetry with D_{4h} as the point group. Because the recent experimental results for Landé factors do not evidence their anisotropy in the plane perpendicular to the tetragonal crystal **c** axis, we use these experimental results and the present **k.p** calculations to determine the Kane energies perpendicular to and along the **c** axis, as well as the Luttinger parameters κ_1 and κ_2 for $MAPbI_3$ and $CsPbBr_3$.

DOI: 10.1103/PhysRevB.106.165201

I. INTRODUCTION

Halide perovskites are very versatile materials with outstanding properties. That is why they have recently been the center of attention in different fields of research. At first, this interest was centered on their photovoltaic properties, leading to a strong and very fast improvement in solar cells efficiencies from 3.8% in 2009 [1] to 29.8% recently in the latest silicon-based tandem cells [2]. In parallel, several studies have been carried out in relation to their optoelectronic properties, concluding in the realization of light emitting diodes even in the blue region [3–5], lasers [6–8], nonlinear devices [9], and photodetectors [10,11]. The synthesis of halide perovskite nanocrystals and nanostructures has also opened the possibility to enlarge their potential applications in cryptography and the quantum information domain [12–14].

Halide perovskites exhibit other very interesting properties which have been less explored until now. The presence of lead and other atoms, such as iodine, is the basis of large spin-orbit coupling (SOC) in these materials. The giant "splitting" of the conduction band instead of the more standard splitting of the valence band is a clear signature of this strong SOC, which will allow optical initialization of electronic spins [15,16] and their manipulation by magnetic [17–19] or electric fields. This strong coupling is also the cause of Rashba spin splittings [20–23] and should be the origin of a strong spin relaxation. Nonetheless, a slow spin relaxation time has been observed due to the presence of localized electrons and holes [18,19,24,25].

Possessing a high SOC and high charge carrier mobility as well as exceptional optical properties, perovskites are also promising candidates for photospintronics applications. When these applications include the use of an applied magnetic field, knowledge of the Landé factors for both the electron and the hole is of prime importance. Experimental studies on bulk or polycrystalline films materials are very sparse [24] and concern mainly $CH_3NH_3PbI_3$ ($MAPbI_3$) [17,19,25–27] and $CsPbBr_3$ [18,28]. An anisotropic Landé factor is obtained in particular for the last two materials. Landé factors for electrons and holes then take different values along the **c** axis of the orthorhombic crystal and perpendicular to the **c** axis. However, while these experiments were carried out at low temperature for a crystal with orthorhombic symmetry, no Landé factor anisotropy was evidenced in the plane perpendicular to the **c** axis (similar to what is expected in a crystal with tetragonal symmetry).

Theoretical studies on the Landé factor are also very sparse but are very important for guiding future experimental and applicative studies. Using an 8-band **k.p** model, calculations for bulk crystal tetragonal symmetry were used some years ago and were applied to $MAPbI_3$ [29]. The main **k.p** parameters were deduced, in this work, from optical absorption experiments, but the result does not completely agree with recent experimental results [25,26]. Calculations with a quasicubic symmetry and tight-binding approaches have also been proposed [28]. In this empirical tight-binding calculation, a large difference from the experiments is obtained. In the **k.p** approach, for $CsPbBr_3$, the authors of Ref. [28] wrote the electron and hole Landé factors as a function of four **k.p** parameters in a quasicubic symmetry. They deduced these **k.p** parameters by fitting their experimental results and found a negative value for the tetragonal crystal field, in disagreement with recent density functional theory (DFT) calculations [30,31]. More recently, an 8-band **k.p** model with an orthorhombic crystal symmetry has been proposed, in a quasicubic approximation [26]. This simplified model uses six parameters, while a complete model requires a much higher number of parameters. For $MAPbI_3$, this approximation leads to tetragonal and orthorhombic crystal fields which are uncorrelated with absorption spectra and optical density [32] or larger than the DFT estimates [33–36].

In this work, because the experimental studies do not show the anisotropy of the electron and hole *g* factors in the plane

*kais.boujdaria@fsb.rnu.tn

 ©2022 American Physical Society

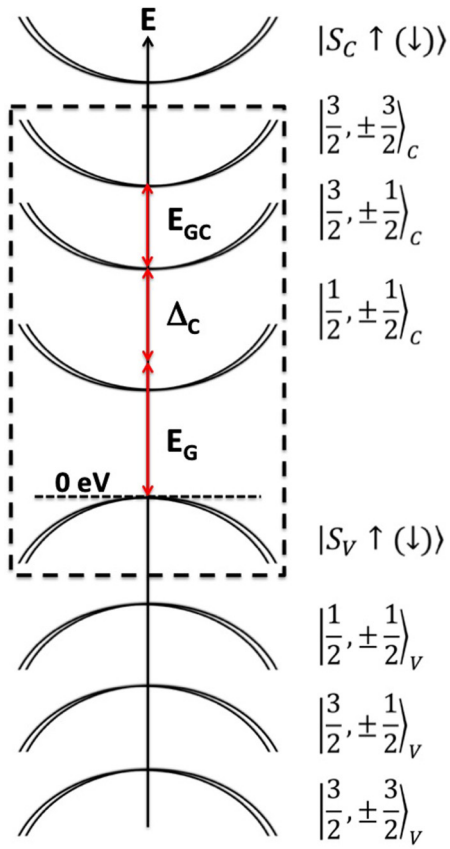

FIG. 1. Schematic representation of the $MAPbI_3$ conduction and valence bands at the Γ point when considering 16 bands. The four first double degenerate valence band states are denoted by $|S_V \uparrow (\downarrow)\rangle$, $|1/2, \pm 1/2\rangle_V$, $|3/2, \pm 1/2\rangle_V$, and $|3/2, \pm 3/2\rangle_V$. The four first double degenerate conduction band states are denoted by $|1/2, \pm 1/2\rangle_C$, $|3/2, \pm 1/2\rangle_C$, $|3/2, \pm 3/2\rangle_C$, and $|S_C \uparrow (\downarrow)\rangle$. The dashed rectangle indicates the involved valence and conduction bands in an 8-band **k.p** model. The band-gap energy E_G and the energy differences (E_{GC}, Δ_C) are also represented. The top of the upper valence band is taken as the energy origin.

perpendicular to the tetragonal **c** axis, we assume that the orthorhombic crystal field is small compared to the tetragonal crystal field. We propose several improvements of the 8-band tetragonal model proposed by Z. G. Yu [29]. First, we will take into account that the tetragonal crystal field is positive rather than negative as Z. G. Yu considered. Second, in the absorption spectrum, we use an identification of optical transitions different from that used in Ref. [29]. Third, we consider a 16-band **k.p** model [37] to calculate the electron and hole Landé factors. This multiband **k.p** approach, applied to tetragonal crystal structure, is compared to the latest experimental results, particularly for bulk inorganic ($CsPbBr_3$) and hybrid ($MAPbI_3$) perovskites.

II. THEORETICAL METHODOLOGY

We apply the **k.p** formalism to calculate the Landé g factors of carriers for halide perovskite with tetragonal crystal structure. To start, it will be useful to recall the main characteristics of the band structure of halide perovskite with a tetragonal lattice.

A. Band structure at the Γ point of halide perovskite with tetragonal crystal structure

Various fundamental studies have been done to describe the band diagram of bulk halide perovskite materials [33,37–41]. In tetragonal $MAPbI_3$ with $I4/mcm$ as the space group and the D_{4h} point group, the conduction and valence band edges are situated at the center of the Brillouin zone. The considered compounds are hence direct band-gap semiconductors in which the upper valence band is mainly built from s orbital symmetry with total angular momentum $j_h = 1/2$ and the lower conduction bands have orbital p symmetry. As previously mentioned, strong SOC affects mainly the conduction band by splitting the electron states into a higher band with total angular momentum $j_e = 3/2$ and a lower band with $j_e = 1/2$, representing the lowest split-off conduction band.

We display in Fig. 1 a schematic representation of the 16-band **k.p** model around the zone center. The model includes the four first valence bands and the four first conduction bands, twice degenerate. The energy at the top of the upper valence band is taken as the origin. The various energy levels represented in Fig. 1 are the band-gap energy E_G and the energy differences (E_{GC}, Δ_C). These basic physical parameters are associated with the interband transition energies from the top valence band state to the conduction states $|\frac{1}{2}, \pm\frac{1}{2}\rangle_C$, $|\frac{3}{2}, \pm\frac{1}{2}\rangle_C$, and $|\frac{3}{2}, \pm\frac{3}{2}\rangle_C$ and are related to the optical transitions (E_1, E_2, E_3) observed in the absorption spectrum and given in Table I via the equations $E_1 = E_G - E_b$, $E_2 = E_G +$

TABLE I. Energies of the optical transitions from the valence states $|S_V \uparrow (\downarrow)\rangle$ to the conduction states $|\frac{1}{2}, \pm\frac{1}{2}\rangle_C$, $|\frac{3}{2}, \pm\frac{1}{2}\rangle_C$, and $|\frac{3}{2}, \pm\frac{3}{2}\rangle_C$, labeled, respectively, E_1, E_2, and E_3, and measured by absorption. E_b denotes the binding energy of bulk perovskite. The energy of the top valence states $|S_V \uparrow (\downarrow)\rangle$ is chosen as origin. $E_{|\frac{1}{2},\pm\frac{1}{2}\rangle_V}$, $E_{|\frac{3}{2},\pm\frac{1}{2}\rangle_V}$, and $E_{|\frac{3}{2},\pm\frac{3}{2}\rangle_V}$ respectively refer to the energies of the valence states $|\frac{1}{2}, \pm\frac{1}{2}\rangle_V$, $|\frac{3}{2}, \pm\frac{1}{2}\rangle_V$, and $|\frac{3}{2}, \pm\frac{3}{2}\rangle_V$.

	Energies (eV)							
	E_1	E_2	E_3	E_b	$E_{\|S_V\uparrow(\downarrow)\rangle}$	$E_{\|\frac{1}{2},\pm\frac{1}{2}\rangle_V}$	$E_{\|\frac{3}{2},\pm\frac{1}{2}\rangle_V}$	$E_{\|\frac{3}{2},\pm\frac{3}{2}\rangle_V}$
$MAPbI_3$	1.633[a]	3.47[a]	3.67[a]	0.016[b]	0	−1.62	−1.88	−1.98
$CsPbBr_3$	2.33[c]	3.68[c]	3.83[c]	0.032[d]	0	−1.82	−1.84	−1.84

[a]Reference [32].
[b]Reference [42].
[c]Reference [44].
[d]Reference [43].

TABLE II. Spin-orbit and crystal field couplings, as well as the phase angle θ, are deduced from the transition energies. The Kane energies $E_{P_{S,\rho}}$ and $E_{P_{S,z}}$ are deduced from the experimental values of the longitudinal ($g_{h\parallel}$) and transverse ($g_{h\perp}$) hole Landé factors and from their theoretical expressions in Eq. (3). $E_{P_{X,1}}$, $E_{P_{X,2}}$, and $E_{P_{X,3}}$ are the energies associated with the coupling between the p-symmetry valence states and the p-symmetry conduction states for $MAPbI_3$ and $CsPbBr_3$, as defined in Ref. [37] and used to deduce the Luttinger parameters κ_1 and κ_2 from the electron Landé factor and Eqs. (14a) and (14b).

	Basic band parameters							
Perovskite	Δ_{SO} (eV)	T (meV)	θ (deg)	$E_{P_{S,\rho}}$ (eV)	$E_{P_{S,z}}$ (eV)	$E_{P_{X,1}}$ (eV)	$E_{P_{X,2}}$ (eV)	$E_{P_{X,3}}$ (eV)
$MAPbI_3$	1.90	319	40.02	11.29[a]	11.96[a]	10.59[b]	2.75[b]	6.29[b]
$CsPbBr_3$	1.38	240	40.19	11.6[a]	14.04[a]	3.11	4.78	2.04

[a]This work.
[b]Reference [37].

Δ_C, and $E_3 = E_G + \Delta_C + E_{GC}$: E_b is the binding energy of bulk $MAPbI_3$ [42] and bulk $CsPbBr_3$ [43]. The absorption and transmission spectra [32,44] can be used to determine the energies E_1, E_2, and E_3. The energies of the valence states [37] are also displayed in Table I.

The tetragonal crystal field T and the SOC Δ_{SO} are related to the band-to-band transition by the following expressions:

$$(E_3 - E_G) = \frac{1}{2}(T + \Delta_{SO}) + \frac{1}{2}(E_2 - E_G),$$
$$(E_2 - E_G) = \sqrt{\Delta_{SO}^2 + T^2 - \frac{2}{3}T\Delta_{SO}}. \quad (1)$$

Both Δ_{SO} and T are associated with the parameter θ by the expression $\tan 2\theta = (2\sqrt{2}\Delta_{SO})/(\Delta_{SO} - 3T)$. The phase angle θ is a fundamental parameter to determine the basis (see Table VI) used to calculate the band diagram of tetragonal perovskite materials with D_{4h} as the point group. Table II contains the values of these parameters obtained from experimental results.

An 8-band **k.p** calculation was used some years ago to determine the main electronic parameters of the $MAPbI_3$ tetragonal crystal phase [29]. In particular, the author obtained, for $MAPbI_3$, $g_{h\parallel} = -0.472$ and $g_{h\perp} = -0.354$ and $g_{e\parallel} = 1.67$ and $g_{e\perp} = 2.281$ for the hole and electron, respectively [the symbol $\parallel$ ($\perp$) means that the magnetic field is parallel (perpendicular) to the **c** axis of the tetragonal crystallographic structure]. In a recent publication, the band structure of a bulk tetragonal $MAPbI_3$ and other organic-inorganic hybrid perovskites were revisited using a 16-band **k.p** model [37]. The main difference from the previous theoretical results of Z. G. Yu [29] is the order of the conduction band states, namely $|j_e, j_{ez}\rangle_C = |3/2, \pm 3/2\rangle_C$ and $|3/2, \pm 1/2\rangle_C$. This inversion of the order is related to the sign of the tetragonal crystal field parameter. As discussed in Ref. [32], recent DFT calculations based on the experimental crystallographic parameters showed that the crystal field parameter has to be positive, not negative, as was considered in Ref. [29]. Based on these insights, we identify in this work the peaks observed in the absorption spectra of $MAPbI_3$ [32] in a different manner than in Ref. [29].

To calculate the Landé g factor, we use the **k.p** theory including the spin (double group in group theory) and show that under a magnetic field **B**, new terms appear in the single-carrier Hamiltonian. Some of them possess the symmetry of an axial vector, giving rise to a coupling $\boldsymbol{\mu}.\mathbf{B}$, with $\boldsymbol{\mu}$ being the magnetic moment. The origin of the Landé g factor and the part of group theory in the determination of the pertinent matrix elements are developed hereafter.

B. Electron and hole Landé factors

The explicit derivation of the Landé factor for conduction electrons and valence holes requires the evaluation of the matrix elements of the $\mathcal{H}_{\mathbf{k.p}} = \frac{\hbar}{m_0}\mathbf{k.p}$ Hamiltonian within the 16-band model [37]. Via the **k.p** operator, the (s, p) conduction bands are mixed with the (s, p) valence bands, and we summarize this coupling following a matrix representation [see Eq. (A1)]. Hence, all the matrix elements needed for computing the Landé factors are given explicitly in Appendix A. In Table VI, we give explicitly the basis functions used to calculate the matrix elements of Eq. (A1) (see Appendix A).

Due to the presence of an external static magnetic field **B**, the kinetic momentum is defined as $(\mathbf{p} + e\mathbf{A})(e > 0$, with e being the elementary charge), where **A** is the vector potential of **B**. Consequently, the components of $\mathbf{k} = (k_x, k_y, k_z)$ no longer commute (leading to the Landé factor):

$$[k_\alpha, k_\beta] = -i\frac{e}{\hbar}\epsilon_{\alpha\beta\gamma}B_\gamma, \quad (2)$$

where $\alpha, \beta, \gamma = x, y, z$ denote the Cartesian components, with $\epsilon_{\alpha\beta\gamma}$ being the antisymmetric tensor of rank 3.

In a tetragonal material, the electron and hole Landé factors are represented by second-rank tensors which can be calculated by using the second-order perturbation theory.

1. The valence band g factors

We use the following Zeeman Hamiltonian: $\mathcal{H}_Z^h = g_h\mu_B\mathbf{S}_h.\mathbf{B}$, where $\mu_B = e\hbar/2m_0$ is the Bohr magneton and $\mathbf{S}_h$ ($s_h = 1/2$) represents the hole angular momentum. Within $\{|S_V \uparrow\rangle, |S_V \downarrow\rangle\}$ subspace and due to the noncommutative relations among **k** components [Eq. (2)], we can write the Zeeman effective Hamiltonian for the valence band [29] as $(\mu_B/2)[g_{h//}\sigma_z B_z + g_{h\perp}(\sigma_x B_x + \sigma_y B_y)]$ [$\boldsymbol{\sigma} = (\sigma_x, \sigma_y, \sigma_z)$ are the spin Pauli matrices]. According to the matrix elements given in Eq. (A1) and employing the Löwdin renormalization [45], we can deduce the elements of the valence band Landé factor tensor along and perpendicular to the **c** axis of the tetragonal structure.

We get

$$g_{h\parallel} = g_0 + E_{P_{S,\rho}}\left[\frac{1}{(E_G+\Delta_C+E_{GC})} - \frac{\sin^2\theta}{(E_G+\Delta_C)} - \frac{\cos^2\theta}{E_G}\right],$$
$$g_{h\perp} = g_0 + \sin\theta\cos\theta\sqrt{2E_{P_{S,\rho}}E_{P_{S,z}}}\left[\frac{1}{(E_G+\Delta_C)} - \frac{1}{E_G}\right], \tag{3}$$

where $g_0 = 2.0023$ is the free electron Landé factor and the energy related to the interband momentum matrix $P_{S,\rho}$ ($P_{S,z}$) is $E_{P_{S,\rho}} = \frac{2m_0}{\hbar^2}P^2_{S,\rho}$ ($E_{P_{S,z}} = \frac{2m_0}{\hbar^2}P^2_{S,z}$). In Appendix A, the definition of the Kane momentum matrix elements ($P_{S,\rho}, P_{S,z}$) is explicitly given. Because the contributions due to $s_V - p_V$ and $s_V - s_C$ couplings are null when the state space is extended, these expressions for the valence band g factors do not change when 8-band or 16-band calculations are considered. The methodology used here to get Eq. (3) is the same as the one reported by L. M. Roth *et al.* [46] for cubic systems. It should be noted that the valence band g factors are mostly caused by the **k.p** interaction with the conduction band [29,46].

2. The conduction-band g factors

According to the derivation in Ref. [47], in the cubic symmetry ($\cos\theta = \sqrt{\frac{2}{3}}; \sin\theta = \frac{1}{\sqrt{3}}; E_{P_{S,\rho}} = E_{P_{S,z}} = E_{P_S}$), the Zeeman Hamiltonian can be written for the p conduction bands:

$$\mathcal{H}^e_Z = \mu_B K\mathbf{L}\cdot\mathbf{B} + \mu_B\boldsymbol{\sigma}\cdot\mathbf{B}, \tag{4}$$

where $\mathbf{L}$ is the angular momentum ($\ell = 1$), $\boldsymbol{\sigma}$ is the spin Pauli operator, $\mathbf{B}$ is the magnetic field, μ_B is the Bohr magneton, and K is a constant induced by the coupling with the bands outside the p conduction bands at higher or lower energy. One commonly uses the Luttinger parameter κ, defined by $K = -(1+3\kappa)$, and rewrites

$$\mathcal{H}^e_Z = -(1+3\kappa)\mu_B\mathbf{L}\cdot\mathbf{B} + \mu_B\boldsymbol{\sigma}\cdot\mathbf{B}. \tag{5}$$

In the absence of coupling, $K = 0$, and $\kappa = -1/3$.

For the lowest conduction band Γ_7, in the cubic symmetry, one has the relations

$$\mathbf{L} = \tfrac{4}{3}\mathbf{J}_e, \quad \boldsymbol{\sigma} = -\tfrac{2}{3}\mathbf{J}_e, \tag{6}$$

with $\mathbf{J}_e$ being an angular momentum that takes the value $j_e = 1/2$. Note the extra factor of 2 in these equations, compared to the expressions in Appendix B of Ref. [47]. This correction has already been noted by other authors [48–50].

One can then write

$$\mathcal{H}^e_Z = -\tfrac{4}{3}(1+3\kappa)\mu_B\mathbf{J}_e\cdot\mathbf{B} - \tfrac{2}{3}\mu_B\mathbf{J}_e\cdot\mathbf{B} = -2\mu_B(1+2\kappa)\mathbf{J}_e\cdot\mathbf{B}. \tag{7}$$

This leads to the electron Landé factors for cubic symmetry:

$$g^C_{e\parallel} = g^C_{e\perp} = -2(1+2\kappa) \tag{8}$$

In absence of coupling with other bands, $\kappa = -1/3$, and $g^C_{e\parallel} = g^C_{e\perp} = -2/3$.

In tetragonal symmetry, one has the relations

$$L_z = 2\cos^2\theta J_{ez}, \quad \sigma_z = -2(\cos^2\theta - \sin^2\theta)J_{ez}, \tag{9a}$$
$$L_{x/y} = 2\sqrt{2}\sin\theta\cos\theta J_{ex/ey}, \quad \sigma_{x/y} = -2\sin^2\theta J_{ex/ey}, \tag{9b}$$

and the Hamiltonian can be written as

$$\mathcal{H}^e_Z = -2\mu_B\begin{bmatrix}[(\cos^2\theta - \sin^2\theta) + (1+3\kappa_1)\cos^2\theta]J_{ez}B_z \\ +[\sin^2\theta + \sqrt{2}\sin\theta\cos\theta(1+3\kappa_2)](J_{ex}B_x + J_{ey}B_y)\end{bmatrix}, \tag{10}$$

where (κ_1, κ_2) are the Luttinger anisotropic factors for tetragonal structures and are associated with the coupling with remote bands from the conduction p bands.

This leads to the Landé factors in tetragonal symmetry for six conduction p bands:

$$g^{T-6b}_{e\parallel} = -2[(\cos^2\theta - \sin^2\theta) + (1+3\kappa_1)\cos^2\theta], \tag{11a}$$
$$g^{T-6b}_{e\perp} = -2[\sin^2\theta + \sqrt{2}\sin\theta\cos\theta(1+3\kappa_2)]. \tag{11b}$$

In the 8-band basis (shown in Fig. 1), one has

$$g^{T-8b}_{e\parallel} = -2\left[(\cos^2\theta - \sin^2\theta) - \frac{E_{Ps,\rho}\cos^2\theta}{2E_G} + (1+3\widetilde{\kappa}_1)\cos^2\theta\right], \tag{12a}$$
$$g^{T-8b}_{e\perp} = -2\left[\sin^2\theta - \frac{\sqrt{2E_{Ps,\rho}E_{Ps,z}}}{2E_G}\sin\theta\cos\theta + \sqrt{2}\sin\theta\cos\theta(1+3\widetilde{\kappa}_2)\right], \tag{12b}$$

where $(\widetilde{\kappa}_1, \widetilde{\kappa}_2)$ are the renormalized Luttinger parameters which describe the interband interactions beyond the ones existing inside the 8-band basis. Note that these expressions are identical to the ones given in Ref. [29], where the Zeeman Hamiltonian was defined as

$$\mathcal{H}^e_Z = -\mu_B(1+3\kappa_1)L_zB_z - \mu_B(1+3\kappa_2)(L_xB_x + L_yB_y) + \mu_B\boldsymbol{\sigma}_e\cdot\mathbf{B}. \tag{13}$$

In the 16-band basis, using the Hamiltonian $\mathcal{H}_Z^e$ and a Löwdin renormalization, it is possible to deduce the contributions due to couplings with lower valence bands. This leads to the following expressions:

$$g_{e\parallel}^{T-16b} = -2(\cos^2\theta - \sin^2\theta) + \frac{E_{P_{S,\rho}}\cos^2\theta}{E_G} - \frac{E_{P_{X,3}}\sin^2\theta}{(E_{|1/2,1/2\rangle_C} - E_{|3/2,\pm3/2\rangle_V})} + \frac{E_{P_{X,3}}\sin^4\theta - E_{P_{X,2}}\cos^4\theta}{(E_{|1/2,1/2\rangle_C} - E_{|3/2,\pm1/2\rangle_V})}$$
$$+ \sin^2\theta\cos^2\theta\frac{E_{P_{X,3}} - E_{P_{X,2}}}{(E_{|1/2,1/2\rangle_C} - E_{|1/2,\pm1/2\rangle_V})} - 2(1+3\overline{\kappa}_1)\cos^2\theta, \tag{14a}$$

$$g_{e\perp}^{T-16b} = -2\sin^2\theta + \sin\theta\cos\theta\frac{\sqrt{2E_{P_{S,\rho}}E_{P_{S,z}}}}{E_G} - \sqrt{2E_{P_{X,1}}E_{P_{X,3}}}\sin\theta\cos\theta$$
$$\times\left[\frac{\sin^2\theta}{(E_{|1/2,1/2\rangle_C} - E_{|3/2,\pm1/2\rangle_V})} + \frac{\cos^2\theta}{(E_{|1/2,1/2\rangle_C} - E_{|1/2,\pm1/2\rangle_V})}\right] - 2\sqrt{2}\sin\theta\cos\theta(1+3\overline{\kappa}_2), \tag{14b}$$

where $(\overline{\kappa}_1, \overline{\kappa}_2)$ are the renormalized Luttinger parameters induced by the coupling with valence and conduction bands outside of the 16-band basis (Table VI) or by higher-order contributions. The related energies $E_{P_{X,i}}$ $(i = 1, 2, 3)$ are given by $E_{P_{X,i}} = (2m_0/\hbar^2)P_{X,i}^2$, with $P_{X,i}$ being the **k.p** matrix elements resulting from the coupling between the p-like valence bands and p-like conduction bands. Note that according to the multiplication tables of the D_{4h} group given in Ref. [51], we have $P_{X,1} = (\hbar/m_0)\langle X_V|p_z|iY_C\rangle = -(\hbar/m_0)\langle Y_V|p_z|iX_C\rangle$, $P_{X,2} = (\hbar/m_0)\langle Z_V|p_x|iY_C\rangle = (\hbar/m_0)\langle Z_V|p_y|iX_C\rangle$, and $P_{X,3} = (\hbar/m_0)\langle Z_C|p_x|iY_V\rangle = -(\hbar/m_0)\langle Z_C|p_y|iX_V\rangle$.

The expressions for the electron and hole masses in the 16-band basis at the band-gap extrema can also be deduced. Appendix B gives the carrier masses, which are defined either along ($\parallel$) or perpendicular to ($\perp$) the **c** axis.

III. THEORY-EXPERIMENT COMPARISON

In this section, we deduce the Kane energies $(E_{P_{S,\rho}}, E_{P_{S,z}})$ and the Luttinger parameter (κ_1, κ_2) for $MAPbI_3$ and $CsPbBr_3$ with tetragonal crystal symmetries. We do this by combining the experimental results from the literature (see Table III) with the current 16-band theory developed for the anisotropic materials to calculate the elements of the Landé g factor tensor.

Experimental studies on the Landé factors of electrons and holes are very few. Table III summarizes the experimental results obtained for $MAPbI_3$ and $CsPbBr_3$ in bulk materials [18,26,28], polycrystalline materials [17,52], and nanocrystals [27,52,53]. There is no experimental proof of anisotropy of the electron or hole Landé factors in the plane perpendicular to the **c** axis.

The authors of Ref. [26] considered an orthorhombic crystallographic structure with a simplified model containing only six parameters. They obtained theoretically anisotropy of in-plane (g_x, g_y) Landé factors that could unambiguously be measured, but experimentally, it has not been observed. That is why, in the following, we use the tetragonal model developed in the previous section to deduce basic fundamental parameters. First, we obtain band parameters from absorption spectra of $MAPbI_3$ and $CsPbBr_3$ bulk materials. Second, by using the general expressions providing the hole Landé factors [see Eq. (3)], we calculate the Kane energies.

A. Band parameters

The fundamental band parameters are summarized in Table II. Some of them are directly extracted from the 16-band **k.p** model as the energies $E_{P_{X,i}}$ $(i = 1, 2, 3)$ related to the interband momentum matrix elements $P_{X,i}$ and the values of the others have been fixed by taking into account experimental results.

Then, to fix the spin-orbit coupling Δ_{SO}, crystal field T, and the phase angle θ, we use the transition energies listed in Table I and Eq. (1). In the $MAPbI_3$ absorption spectrum measured by Hirasawa *et al.* [32], we have identified the following energies: $E_G + \Delta_C + E_{GC} = E_3 = 3.67$ eV, $E_G + \Delta_C = E_2 = 3.47$ eV, and $E_G = E_1 + E_b = 1.65$ eV. We have associated the absorption peak at 2.75 eV with the X-point optical transition rather than the Γ-point transition as done by Z. G. Yu [29]. We found a positive T value splitting that was higher than that found in previous DFT calculations [31,34,35] and had a sign opposite that found in Ref. [29]. Δ_{SO} is larger than the value obtained in DFT calculations.

We calculate T and Δ_{SO} once again by applying Eq. (1) and injecting the bulk $CsPbBr_3$ experimental transition energies

TABLE III. Experimental values of Landé factors for different types of $MAPbI_3$ and $CsPbBr_3$ nanomaterials.

$MAPbI_3$	$g_{h\parallel}$	$g_{h\perp}$	$g_{e\parallel}$	$g_{e\perp}$
Bulk[a]	−0.28	−0.71	2.46	2.98
Bulk[b]	−0.28	−0.57	2.52	2.63
Polycrystal[c]	−0.33		2.63	
Polycrystal[d]	−0.299	−0.406	1.604	2.6
$CsPbBr_3$	$g_{h\parallel}$	$g_{h\perp}$	$g_{e\parallel}$	$g_{e\perp}$
Bulk[e]		0.75		1.96
Bulk[a]	0.85	0.65	1.69	2.06
Nanocrystals[f]	0.83		1.73	
Polycrystal[f]	0.77		1.78	
Nanocrystals[g]	0.8		1.8	

[a]Reference [28].
[b]Reference [26].
[c]Reference [17].
[d]Reference [27].
[e]Reference [18].
[f]Reference [52].
[g]Reference [53].

derived from Ref. [44] ($E_3 = 3.83$ eV, $E_2 = 3.68$ eV, $E_1 = 2.37$ eV; see Table I). The calculated T value is higher than or comparable to the values from DFT calculations [31], and Δ_{SO} is slightly smaller in our case than in DFT calculations.

In the next section, we describe how we have deduced from the experimental values given in Table III the Kane energies ($E_{P_{S,\rho}}, E_{P_{S,z}}$) for $MAPbI_3$ and $CsPbBr_3$ given in Table II.

B. The Kane energies ($E_{P_{S,\rho}}, E_{P_{S,z}}$)

By using theoretical expressions (3) and the experimentally determined hole g factors (see Table III), we deduce the Kane energies ($E_{P_{S,\rho}}, E_{P_{S,z}}$). Note that in Ref. [28], the authors also measured the components of the Landé tensor in the $MAPbI_3$ crystal but we do not make a comparison with these experimental results because the authors highlighted that the main axes are tilted with respect to the cubic axes and underlined the possibility of a monoclinic phase or a rotation of the crystallographic axes with respect to the laboratory frame. Using the hole Landé factor of Ref. [26] for $MAPbI_3$ and Ref. [28] for $CsPbBr_3$, we obtained ($E_{P_{S,\rho}} = 11.29$ eV, $E_{P_{S,z}} = 11.96$ eV) and ($E_{P_{S,\rho}} = 11.6$ eV, $E_{P_{S,z}} = 14.04$ eV), respectively. These values are of the same order of magnitude but smaller than theoretical values previously derived via **k.p** calculations for a tetragonal crystal symmetry [37,54]. These Kane energies are also less anisotropic than the ones for $CsPbBr_3$ found in the supplementary information of Ref. [28], namely, $E_{P_{S,\rho}} = 11.2$ eV and $E_{P_{S,z}} = 16.4$ eV.

When we compare the values of the parameters used in Eq. (3) for $MAPbI_3$ and for $CsPbBr_3$, we underline that the Kane energies and the phase angle θ have comparable values in both perovskite materials. The principal variations relate to the band-gap energy E_G and Δ_C.

We also want to emphasize that the Kane energy values estimated from the experimental results for the Landé factors are smaller than the theoretical predictions obtained for cubic materials [43,55] and compatible but slightly smaller than the calculated values for a tetragonal crystal structure [37]. Based on these findings, we propose in Fig. 2 a general expression for how $g_{h\parallel}$ and $g_{h\perp}$ are related to the band-gap energy. A linear interpolation between the values for $MAPbI_3$ and $CsPbBr_3$ yields the value Δ_C. We also draw the conclusion that all iodine perovskites, whether organic or inorganic, exhibit a negative value for g_h, but all bromide or chloride perovskites exhibit a positive value for g_h. An experimental study done recently supports that conclusion [28].

C. The Luttinger parameters (κ_1, κ_2)

The experimentally measured electron g factors and expressions (12a) and (12b) for the 8-band model can be used to get the Luttinger parameters. In order to employ the 16-band equations (14a) and (14b), we need to know the energies of the valence states (obtained using the 16-band **k.p** model) and conduction states (extracted from optical absorption measurements; see Table I), as well as the Kane energies related to the $p_C - p_V$ mixing for $MAPbI_3$ and $CsPbBr_3$ (see Table II). Once the various Landé tensor components have been numerically evaluated, we compare them to the experimental data (Ref. [26] for $MAPbI_3$ and Ref. [18] for $CsPbBr_3$) and derive

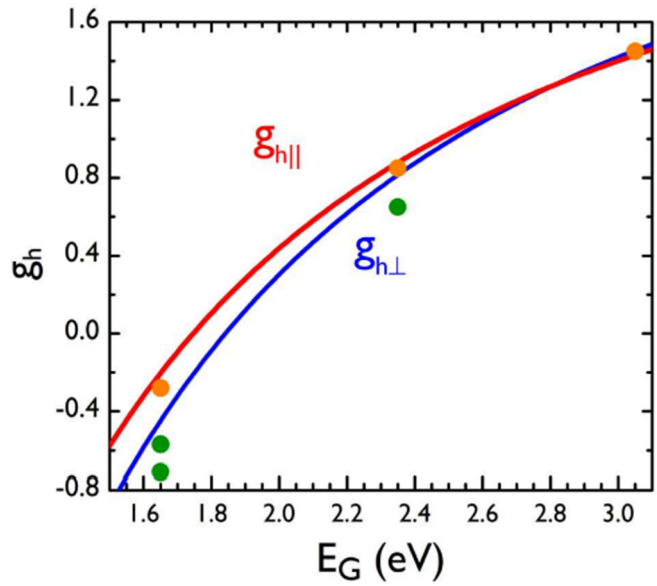

FIG. 2. Hole Landé factors vs the band-gap energy E_G. The red line represents the values obtained with the proposed universal expression for $g_{h\parallel}$ [see Eq. (3)] with $\theta = 40°$ and $E_{P_{s,\rho}} = 11$ eV. The blue line represents the values obtained with the expression for $g_{h\perp}$ [see Eq. (3)] with $E_{P_{s,\rho}} = E_{P_{s,z}} = 11$ eV. Δ_C is obtained by linear interpolation of Δ_C between the $MAPbI_3$ and $CsPbBr_3$ values: $\Delta_C = 2.98 - 0.7E_G$. The green circles represent the experimental values of $g_{h\perp}$ determined in bulk $MAPbI_3$ [26] and bulk $CsPbBr_3$ [28]. The orange circles represent the experimental values of $g_{h\parallel}$ obtained in bulk $MAPbI_3$ [26] and bulk $CsPbBr_3$ [28] and g_h in bulk $CsPb(Br_{0.05}Cl_{0.95})$ [28].

the Luttinger parameters in both configurations: 8 bands for evaluating ($\tilde{\kappa}_1, \tilde{\kappa}_2$) and 16 bands for calculating ($\bar{\kappa}_1, \bar{\kappa}_2$).

The calculated values for 8-band and 16-band models for $MAPbI_3$ and $CsPbBr_3$ are listed in Table IV, together with the obtained Luttinger parameters. We underline that the corrections provided by taking 16-band calculations into account are

TABLE IV. Electron Landé g factors calculated from Eqs. (12a) and (12b) in the 8-band configuration and from Eqs. (14a) and (14b) in the 16-band configuration in the absence of the Luttinger correction ($\tilde{\kappa}_i = \bar{\kappa}_i = -1/3$, $i = 1, 2$) and Luttinger parameters extracted from the experimental data using the 8-band model ($\tilde{\kappa}_1, \tilde{\kappa}_2$) and 16-band model ($\bar{\kappa}_1, \bar{\kappa}_2$).

	Electron Landé g factors			
	8-band model		16-band model	
	$g_{e\parallel}$	$g_{e\perp}$	$g_{e\parallel}$	$g_{e\perp}$
$MAPbI_3$	3.67	4.08	3.25	2.39
$CsPbBr_3$	2.53	2.94	1.87	2.52
	Luttinger parameters			
	8-band model		16-band model	
	$\tilde{\kappa}_1$	$\tilde{\kappa}_2$	$\bar{\kappa}_1$	$\bar{\kappa}_2$
$MAPbI_3$	−0.007	0.013	−0.126	−0.39
$CsPbBr_3$	−0.092	−0.124	−0.282	−0.224

TABLE V. Electron and hole masses deduced from the 16-band **k.p** modelization for $MAPbI_3$ and $CsPbBr_3$. Carrier masses deduced from the DFT calculation for tetragonal symmetry and with spin-orbit coupling are also given. The reduced effective exciton masses are also provided and can be compared with experimental results.

	$MAPbI_3$		$CsPbBr_3$	
Mass (in units of m_0)	**k.p**	DFT	**k.p**	DFT
$m_{e\parallel}$	0.171	0.20[a]	0.204	0.17[b]
$m_{e\perp}$	0.251	0.26[a]	0.337	0.28[b]
$m_{h\parallel}$	0.249	0.23[a]	0.27	0.21[b]
$m_{h\perp}$	0.311	0.26[a]	0.384	0.24[b]
$\mu_\parallel$	0.101	0.11[a]	0.116	0.09[b]
$\mu_\perp$	0.139	0.13[a]	0.179	0.13[b]
$\mu_{\rm exp}$	0.104[c]		0.126[d]	

[a]Reference [59].
[b]Reference [60].
[c]Reference [56].
[d]Reference [57].

not negligible and allow us to improve the agreement between theory and experiments. We note that the correction beyond 8 or 16 bands is smaller as κ_1 and κ_2 values are close to a value of $-1/3$. The results for Landé factors for the electron and hole extracted from the 16-band **k.p** model with tetragonal symmetry are closer to the experimental results than the ones determined in the cubic approximation or tetragonal symmetry with only an 8-band **k.p** model.

D. The electron and hole masses

Having estimated the 16-band parameters for $MAPbI_3$ and $CsPbBr_3$, it is then possible to determine the expected electron and hole masses from Eqs. (B1)–(B4) by using the parameters from Tables I and II. The calculated masses are given in Table V.

The masses deduced from the **k.p** analysis are in good agreement with both experimental measurements of the reduced exciton mass $\mu_{\rm exp}$ [56,57] and recent DFT calculations that include spin-orbit coupling (generalized gradient approximation+SOC) in the tetragonal phases [58].

Our **k.p** values for $MAPbI_3$ compare favorably to the masses obtained by Traore *et al.* [59]. Very recently, Su *et al.* [60] derived the carrier masses for the tetragonal phase in $CsPbBr_3$. They found carrier masses which are consistent with our **k.p** estimates, with both theories predicting mass anisotropy.

IV. CONCLUSION

In a 16-band **k.p** modelization, we derived the electron and hole g factors for tetragonal halide perovskites and compared them to very recent experiments. The computed Kane energies are slightly lower than the experimental results when compared to the results of the **k.p** calculations. For $MAPbI_3$ ($CsPbBr_3$), we derived $E_{P_{S,\rho}} = 11.29$ eV (11.6 eV) and $E_{P_{S,z}} = 11.96$ eV (14.04 eV). Extending this analysis, we provided an expression for the two values of the hole g factors (parallel and perpendicular to the tetragonal crystal axis) as a function of the band-gap energy that is applicable to all halide perovskite materials. The hole g factor is tuned from negative values to positive values by increasing the band-gap energy, i.e., by switching the halide atom from iodine to bromine or chlorine in the $APbX_3$ perovskite bulk materials (A=Cs, FA, or MA; X=I, Br, or Cl). We showed that the use of 16-band contributions to the electron g factors improves the agreement between theory and experiments and leads to Luttinger parameters κ_1 and κ_2 closer to values of $-1/3$, corresponding to the absence of contributions beyond 16 bands. Finally, the same **k.p** parameters in the 16-band **k.p** framework offer an opportunity to predict electron and hole masses in good agreement with experimental results and DFT prediction.

ACKNOWLEDGMENTS

This work was financially supported by the Tunisian Ministry of Higher Education and Scientific Research, the French Ministry of Foreign Affairs through the project PHC Utique (Grant No. 22G1305), and the French National Research Agency (Grant No. ANR IPER-Nano2, ANR- 18-CE30-0023).

APPENDIX A: MATRIX COUPLING

We present in detail the necessary matrix elements for evaluating the electron and hole Landé factors within a 16-band **k.p** model for the tetragonal crystal with D_{4h} as the point

TABLE VI. Basis functions near the zone center used to calculate the coupling matrix [see Eq. (A1)].

Conduction band states	Valence band states
$\lvert C_+\rangle = \lvert S_C\uparrow\rangle$	$\lvert V_1\rangle = \lvert S_V\uparrow\rangle$
$\lvert\frac{3}{2},\frac{3}{2}\rangle_C = i[\lvert\frac{-1}{\sqrt{2}}(X_C+iY_C)\uparrow\rangle]$	$\lvert\frac{3}{2},\frac{3}{2}\rangle_V = i[\lvert\frac{-1}{\sqrt{2}}(X_V+iY_V)\uparrow\rangle]$
$\lvert\frac{3}{2},-\frac{3}{2}\rangle_C = i[\lvert\frac{1}{\sqrt{2}}(X_C-iY_C)\downarrow\rangle]$	$\lvert\frac{3}{2},-\frac{3}{2}\rangle_V = i[\lvert\frac{1}{\sqrt{2}}(X_V-iY_V)\downarrow\rangle]$
$\lvert\frac{3}{2},\frac{1}{2}\rangle_C = i[\lvert-\frac{\sin\theta}{\sqrt{2}}(X_C+iY_C)\downarrow+\cos\theta Z_C\uparrow\rangle]$	$\lvert\frac{3}{2},\frac{1}{2}\rangle_V = i[\lvert-\frac{\sin\theta}{\sqrt{2}}(X_V+iY_V)\downarrow+\cos\theta Z_V\uparrow\rangle]$
$\lvert\frac{3}{2},-\frac{1}{2}\rangle_C = i[\lvert\frac{\sin\theta}{\sqrt{2}}(X_C-iY_C)\uparrow+\cos\theta Z_C\downarrow\rangle]$	$\lvert\frac{3}{2},-\frac{1}{2}\rangle_V = i[\lvert\frac{\sin\theta}{\sqrt{2}}(X_V-iY_V)\uparrow+\cos\theta Z_V\downarrow\rangle]$
$\lvert\frac{1}{2},\frac{1}{2}\rangle_C = i[\lvert-\frac{\cos\theta}{\sqrt{2}}(X_C+iY_C)\downarrow-\sin\theta Z_C\uparrow\rangle]$	$\lvert\frac{1}{2},\frac{1}{2}\rangle_V = i[\lvert-\frac{\cos\theta}{\sqrt{2}}(X_V+iY_V)\downarrow-\sin\theta Z_V\uparrow\rangle]$
$\lvert\frac{1}{2},-\frac{1}{2}\rangle_C = -i[\lvert\frac{\cos\theta}{\sqrt{2}}(X_C-iY_C)\uparrow-\sin\theta Z_C\downarrow\rangle]$	$\lvert\frac{1}{2},-\frac{1}{2}\rangle_V = -i[\lvert\frac{\cos\theta}{\sqrt{2}}(X_V-iY_V)\uparrow-\sin\theta Z_V\downarrow\rangle]$
$\lvert C_-\rangle = \lvert S_C\downarrow\rangle$	$\lvert V_2\rangle = \lvert S_V\downarrow\rangle$

group. Within the basis explicitly given in Table VI, we get

$$\begin{bmatrix} & \left|\frac{3}{2}\frac{3}{2}\right\rangle_C & \left|\frac{3}{2}\frac{-3}{2}\right\rangle_C & \left|\frac{3}{2}\frac{1}{2}\right\rangle_C & \left|\frac{3}{2}\frac{-1}{2}\right\rangle_C & \left|\frac{1}{2}\frac{1}{2}\right\rangle_C & \left|\frac{1}{2}\frac{-1}{2}\right\rangle_C & |S_C\uparrow\rangle & |S_C\downarrow\rangle \\ \left\langle\frac{3}{2}\frac{3}{2}\right|_V & P^z_{X,1} & 0 & \frac{-P^-_{X,3}}{\sqrt{2}}\cos\theta & 0 & \frac{P^-_{X,3}}{\sqrt{2}}\sin\theta & 0 & \frac{-P^+_\rho}{\sqrt{2}} & 0 \\ \left\langle\frac{3}{2}\frac{-3}{2}\right|_V & 0 & -P^z_{X,1} & 0 & \frac{-P^+_{X,3}}{\sqrt{2}}\cos\theta & 0 & \frac{-P^+_{X,3}}{\sqrt{2}}\sin\theta & 0 & \frac{P^-_\rho}{\sqrt{2}} \\ \left\langle\frac{3}{2}\frac{1}{2}\right|_V & \frac{-P^-_{X,2}}{\sqrt{2}}\cos\theta & 0 & P^z_{X,1}\sin^2\theta & \mathcal{A} & P^z_{X,1}\frac{\sin 2\theta}{2} & -\mathcal{B} & P^z_z\cos\theta & \frac{-1}{\sqrt{2}}P^+_\rho\sin\theta \\ \left\langle\frac{3}{2}\frac{-1}{2}\right|_V & 0 & \frac{-P^+_{X,2}}{\sqrt{2}}\cos\theta & \mathcal{A}^* & -P^z_{X,1}\sin^2\theta & \mathcal{B}^* & P^z_{X,1}\frac{\sin 2\theta}{2} & \frac{1}{\sqrt{2}}P^-_\rho\sin\theta & P^z_z\cos\theta \\ \left\langle\frac{1}{2}\frac{1}{2}\right|_V & \frac{P^-_{X,2}}{\sqrt{2}}\sin\theta & 0 & P^z_{X,1}\frac{\sin 2\theta}{2} & \mathcal{C} & P^z_{X,1}\cos^2\theta & \mathcal{A} & -P^z_z\sin\theta & \frac{-1}{\sqrt{2}}P^+_\rho\cos\theta \\ \left\langle\frac{1}{2}\frac{-1}{2}\right|_V & 0 & \frac{-P^+_{X,2}}{\sqrt{2}}\sin\theta & -\mathcal{C}^* & P^z_{X,1}\frac{\sin 2\theta}{2} & \mathcal{A}^* & -P^z_{X,1}\cos^2\theta & \frac{-1}{\sqrt{2}}P^-_\rho\cos\theta & P^z_z\sin\theta \\ \langle S_V\uparrow| & \frac{-1}{\sqrt{2}}P^+_{S,\rho} & 0 & P^z_{S,z}\cos\theta & \frac{1}{\sqrt{2}}P^-_{S,\rho}\sin\theta & -P^z_{S,z}\sin\theta & \frac{-1}{\sqrt{2}}P^-_{S,\rho}\cos\theta & 0 & 0 \\ \langle S_V\downarrow| & 0 & \frac{1}{\sqrt{2}}P^-_{S,\rho} & \frac{-1}{\sqrt{2}}P^+_{S,\rho}\sin\theta & P^z_{S,z}\cos\theta & \frac{-1}{\sqrt{2}}P^+_{S,\rho}\cos\theta & P^z_{S,z}\sin\theta & 0 & 0 \end{bmatrix}, \tag{A1}$$

where $P^\pm = Pk_\pm = P(k_x \pm ik_y)$ and $P^z = Pk_z$. For example, $\frac{-P^-_{X,3}}{\sqrt{2}}\cos\theta = \frac{-P_{X,3}}{\sqrt{2}}(k_x - ik_y)\cos\theta$, and $P^z_{X,1} = P_{X,1}k_z$. We note $\mathcal{A} = -\frac{\sin\theta\cos\theta}{\sqrt{2}}[P^-_{X,3} + P^+_{X,2}]$, $\mathcal{B} = \frac{1}{\sqrt{2}}[P^-_{X,3}\sin^2\theta - P^+_{X,2}\cos^2\theta]$, and $\mathcal{C} = \frac{1}{\sqrt{2}}[P^+_{X,2}\sin^2\theta - P^-_{X,3}\cos^2\theta]$.

We define the matrix elements associated with the operator $(\frac{\hbar}{m_0}\mathbf{k.p})$ as $P_{S,\rho} = (\hbar/m_0)\langle S_V|p_x|iX_C\rangle = (\hbar/m_0)\langle S_V|p_y|iY_C\rangle$, $P_{S,z} = (\hbar/m_0)\langle S_V|p_z|iZ_C\rangle$; $P_\rho = (\hbar/m_0)\langle S_C|p_x|iX_V\rangle = -(\hbar/m_0)\langle S_C|p_y|iY_V\rangle$, $P_z = (\hbar/m_0)\langle S_C|p_z|iZ_V\rangle$; and $P_{X,1} = (\hbar/m_0)\langle X_V|p_z|iY_C\rangle = -(\hbar/m_0)\langle Y_V|p_z|iX_C\rangle$, $P_{X,2} = (\hbar/m_0)\langle Z_V|p_x|iY_C\rangle = (\hbar/m_0)\langle Z_V|p_y|iX_C\rangle$, and $P_{X,3} = (\hbar/m_0)\langle Z_C|p_x|iY_V\rangle = -(\hbar/m_0)\langle Z_C|p_y|iX_V\rangle$.

We use $E_{P_j} = \frac{2m_0}{\hbar^2}P_j^2$ to define the energy corresponding to the P_j elements of the interband momentum matrix. Thus, $E_{P_{S,\rho}} = \frac{2m_0}{\hbar^2}P^2_{S,\rho}$, $E_{P_{S,z}} = \frac{2m_0}{\hbar^2}P^2_{S,z}$, $E_{P_\rho} = \frac{2m_0}{\hbar^2}P^2_\rho$, $E_{P_z} = \frac{2m_0}{\hbar^2}P^2_z$, $E_{P_{X,1}} = \frac{2m_0}{\hbar^2}P^2_{X,1}$, $E_{P_{X,2}} = \frac{2m_0}{\hbar^2}P^2_{X,2}$, and $E_{P_{X,3}} = \frac{2m_0}{\hbar^2}P^2_{X,3}$.

All the matrix elements associated with the operator $(\frac{\hbar}{m_0}\mathbf{k.p})$ are considered a set of real-valued, adjustable parameters.

APPENDIX B: THE CARRIER EFFECTIVE MASSES

The carrier effective masses also become anisotropic due to the anisotropy of the halide perovskites which are the subject of this study. For the lowest conduction band, the electron effective mass parallel (perpendicular) to the **c** axis is denoted as $m_{e\parallel}$ ($m_{e\perp}$). Similarly, in the upper valence band, $m_{h\parallel}(m_{h\perp})$ represents the hole effective mass parallel to (perpendicular to) the **c** axis.

The electron and hole effective masses are formulated as follows in the framework of the 16-band **k.p** model and the second-order Löwdin perturbation theory [45]:

$$\frac{m_0}{m_{e\parallel}} = 1 + \sin^2\theta\frac{E_{P_{S,z}}}{(E_{|1/2,\pm1/2\rangle_C} - E_{|S_V\uparrow\rangle})} + \cos^2\theta\, E_{P_{X,1}}\left[\frac{\cos^2\theta}{(E_{|1/2,\pm1/2\rangle_C} - E_{|1/2,1/2\rangle_V})} + \frac{\sin^2\theta}{(E_{|1/2,\pm1/2\rangle_C} - E_{|3/2,1/2\rangle_V})}\right], \tag{B1}$$

$$\frac{m_0}{m_{e\perp}} = 1 + \frac{\cos^2\theta}{2}\left[\frac{E_{P_{S,\rho}}}{(E_{|1/2,\pm1/2\rangle_C} - E_{|S_V\downarrow\rangle})} + E_{P_{X,2}}\left(\frac{\sin^2\theta}{(E_{|1/2,\pm1/2\rangle_C} - E_{|1/2,-1/2\rangle_V})} + \frac{\cos^2\theta}{(E_{|1/2,\pm1/2\rangle_C} - E_{|3/2,-1/2\rangle_V})}\right)\right]$$
$$+ \frac{\sin^2\theta}{2}E_{P_{X,3}}\left[\frac{1}{(E_{|1/2,\pm1/2\rangle_C} - E_{|3/2,3/2\rangle_V})} + \frac{\sin^2\theta}{(E_{|1/2,\pm1/2\rangle_C} - E_{|3/2,-1/2\rangle_V})} + \frac{\cos^2\theta}{(E_{|1/2,\pm1/2\rangle_C} - E_{|1/2,-1/2\rangle_V})}\right], \tag{B2}$$

$$\frac{m_0}{m_{h\parallel}} = -1 + E_{P_{S,z}}\left[\frac{\sin^2\theta}{(E_{|S_V\uparrow(\downarrow)\rangle} - E_{|1/2,1/2\rangle_C})} + \frac{\cos^2\theta}{(E_{|S_V\uparrow(\downarrow)\rangle} - E_{|3/2,1/2\rangle_C})}\right], \tag{B3}$$

$$\frac{m_0}{m_{h\perp}} = -1 + \frac{E_{P_{S,\rho}}}{2}\left[\frac{1}{(E_{|S_V\uparrow(\downarrow)\rangle} - E_{|3/2,3/2\rangle_C})} + \frac{\sin^2\theta}{(E_{|S_V\uparrow(\downarrow)\rangle} - E_{|3/2,-1/2\rangle_C})} + \frac{\cos^2\theta}{(E_{|S_V\uparrow(\downarrow)\rangle} - E_{|1/2,-1/2\rangle_C})}\right]. \tag{B4}$$

[1] A. Kojima, K. Teshima, Y. Shirai, and T. Miyasaka, J. Am. Chem. Soc. **131**, 6050 (2009).

[2] A. Al-Ashouri, E. Köhnen, B. Li, A. Magomedov, H. Hempel, P. Caprioglio, J. A. Márquez, A. B. M. Vilches, E. Kasparavicius, J. A. Smith, N. Phung, D. Menzel, M. Grischek, L. Kegelmann, D. Skroblin, C. Gollwitzer, T. Malinauskas, M. Jošt, G. Matič, B. Rech, R. Schlatmann, M. Topič, L. Korte, A. Abate, B. Stannowski, D. Neher, M. Stolterfoht, T. Unold, V. Getautis, and S. Albrecht, Science **370**, 1300 (2020).

[3] M. Lu, Y. Zhang, S. Wang, J. Guo, W. W. Yu, and A. L. Rogach, Adv. Funct. Mater. **29**, 1902008 (2019).

[4] X.-K. Liu, W. Xu, S. Bai, Y. Jin, J. Wang, R. H. Friend, and F. Gao, Nat. Mater. **20**, 10 (2021).

[5] M. Karlsson, Z. Yi, S. Reichert, X. Luo, W. Lin, Z. Zhang, C. Bao, R. Zhang, S. Bai, G. Zheng, P. Teng, L. Duan, Y. Lu, K. Zheng, T. Pullerits, C. Deibel, W. Xu, R. Friend, and F. Gao, Nat. Commun. **12**, 361 (2021).

[6] G. Xing, N. Mathews, S. S. Lim, N. Yantara, X. Liu, D. Sabba, M. Grätzel, S. Mhaisalkar, and T. C. Sum, Nat. Mater. **13**, 476 (2014).

[7] H. Zhu, Y. Fu, F. Meng, X. Wu, Z. Gong, Q. Ding, M. V. Gustafsson, M. T. Trinh, S. Jin, and X.-Y. Zhu, Nat. Mater. **14**, 636 (2015).

[8] L. Lei, Q. Dong, K. Gundogdu, and F. So, Adv. Funct. Mater. **31**, 2010144 (2021).

[9] W. Shen, J. Chen, J. Wu, X. Li, and H. Zeng, ACS Photonics **8**, 113 (2021).

[10] L. Dou, Y. M. Yang, J. You, Z. Hong, W. Chang, G. Li, and Y. Yang, Nat. Commun. **5**, 5404 (2014).

[11] Y. Wang, L. Song, Y. Chen, and W. Huang, ACS Photonics **7**, 10 (2020).

[12] Y.-S. Park, S. Guo, N. S. Makarov, and V. I. Klimov, ACS Nano **9**, 10386 (2015).

[13] G. Rainò, G. Nedelcu, L. Protesescu, M. I. Bodnarchuk, M. V. Kovalenko, R. F. Mahrt, and T. Stöferle, ACS Nano **10**, 2485 (2016).

[14] F. P. Garcia de Arquer, D. V. Talapin, V. I. Klomov, Y. Arakawa, M. Bayer, and E. H. Sargent, Science **373**, eaaz8541 (2021).

[15] D. Giovanni, H. Ma, J. Chua, M. Grätzel, R. Ramesh, S. Mhaisalkar, N. Mathews, and T. C. Sum, Nano Lett. **15**, 1553 (2015).

[16] W. Zhao, R. Su, Y. Huang, J. Wu, C. F. Fong, J. Feng, and Q. Xiong, Nat. Commun. **11**, 5665 (2020).

[17] P. Odenthal, W. Talmadge, N. Gundlach, R. Wang, C. Zhang, D. Sun, Z.-G. Yu, Z. V. Vardeny, and Y. S. Li, Nat. Phys. **13**, 894 (2017).

[18] V. V. Belykh, D. Y. Yakovlev, M. M. Glazov, P. S. Grigoryev, M. Hussain, J. Rautert, D. N. Dirin, M. V. Kovalenko, and M. Bayer, Nat. Commun. **10**, 673 (2019).

[19] G. Garcia-Arellano, G. Trippé-Allard, L. Legrand, T. Barisien, D. Garrot, E. Deleporte, F. Bernardot, C. Testelin, and M. Chamarro, J. Phys. Chem. Lett. **12**, 8272 (2021).

[20] M. Kepenekian, R. Robles, C. Katan, D. Sapori, L. Pedesseau, and J. Even, ACS Nano **9**, 11557 (2015).

[21] M. Kepenekian and J. Even, J. Phys. Chem. Lett. **8**, 3362 (2017).

[22] D. Niesner, M. Wilhelm, I. Levchuk, A. Osvet, S. Shrestha, M. Batentschuk, C. Brabec, and T. Fauster, Phys. Rev. Lett. **117**, 126401 (2016).

[23] Z. Huang, S. R. Vardeny, T. Wang, Z. Ahmad, A. Chanana, E. Vetter, S. Yang, X. Liu, G. Galli, A. Amassian, Z. V. Vardeny, and D. Sun, Appl. Phys. Rev. **8**, 031408 (2021).

[24] E. Kirstein, D. R. Yakovlev, M. M. Glazov, E. Evers, E. A. Zhukov, V. V. Belykh, D. Kopteva, N. E. Kudlacik, O. Nazarenko, D. N. Dirin, M. V. Kovalenko, and M. Bayer, Adv. Mater. **34**, 2105263 (2022).

[25] E. Kirstein, D. R. Yakovlev, E. A. Zhukov, J. Höcker, V. Dyakonov, and M. Bayer, ACS Photonics **9**, 1375 (2022).

[26] U. N. Huynh, Y. Liu, A. Chanana, D. R. Khanal, P. C Sercel, J. Huang, and Z. V. Vardeny, Nat. Commun. **13**, 1428 (2022).

[27] G. Garcia-Arellano, G. Trippé-Allard, T. Campos, F. Bernardot, L. Legrand, D. Garrot, E. Deleporte, C. Testelin, and M. Chamarro, Nanomaterials **12**, 1399 (2022).

[28] E. Kirstein, D. R. Yakovlev, M. M. Glazov, E. A. Zhukov, D. Kudlacik, I. V. Kalitukha, V. F. Sapega, G. S. Dimitriev, M. A. Semina, M. O. Nestoklon, E. L. Ivchenko, N. E. Kopteva, D. N. Dirin, O. Nazarenko, M. V. Kovalenko, A. Baumann, J. Höcker, V. Dyakonov, and M. Bayer, Nat. Commun. **13**, 3062 (2022).

[29] Z. G. Yu, Sci. Rep. **6**, 28576 (2016).

[30] P. C. Sercel, J. L. Lyons, D. Wickramaratne, R. Vaxenburg, N. Bernstein, and A. L. Efros, Nano Lett. **19**, 4068 (2019).

[31] P. C. Sercel, J. L. Lyons, N. Bernstein, and A. L. Efros, J. Chem. Phys. **151**, 234106 (2019).

[32] M. Hirasawa, T. Ishihara, and T. Goto, J. Phys. Soc. Jpn. **63**, 3870 (1994).

[33] J. Even, L. Pedesseau, J-M. Jancu, and C. Katan, J. Phys. Chem. Lett. **4**, 2999 (2013).

[34] R. A. Jishi, O. B. Ta, and A. A. Sharif, J. Phys. Chem. C **118**, 28344 (2014).

[35] W. Geng, L. Zhang, Y.-N. Zhang, W.-M. Lau, and L.-M. Liu, J. Phys. Chem. C **118**, 19565 (2014).

[36] T. Baikie, Y. Fang, J. M. Kadro, M. Schreyer, F. Wei, S. G. Mhaisalkar, M. Graetzeld, and T. J. White, J. Mater. Chem. A **1**, 5628 (2013).

[37] R. Ben Aich, S. Ben Radhia, K. Boujdaria, M. Chamarro, and C. Testelin, J. Phys. Chem. Lett. **11**, 808 (2020).

[38] F. Brivio, K. T. Butler, A. Walsh, and M. van Schilfgaarde, Phys. Rev. B **89**, 155204 (2014).

[39] W.-J. Yin, J.-H. Yang, J. Kang, Y. Yan, and S.-W. Wei, J. Mater. Chem. A **3**, 8926 (2015).

[40] L.-Y. Huang and W. R. L. Lambrecht, Phys. Rev. B **93**, 195211 (2016).

[41] M. Shirayama, H. Kadowaki, T. Miyadera, T. Sugita, M. Tamakoshi, M. Kato, T. Fujiseki, D. Murata, S. Hara, T. N. Murakami, S. Fujimoto, M. Chikamatsu, and H. Fujiwara, Phys. Rev. Appl. **5**, 014012 (2016).

[42] K. Galkowski, A. Mitioglu, A. Miyata, P. Plochocka, O. Portugall, G. E. Eperon, J. Wang, T. Stergiopoulos, S. D. Stranks, H. J. Snaith, and R. J. Nicholas, Energy Environ. Sci. **9**, 962 (2016).

[43] V. Steinmetz, J. Ramade, L. Legrand, T. Barisien, F. Bernardot, E. Lhuillier, M. Bernard, M. Vabre, I. Saidi, A. Ghribi, K. Boujdaria, C. Testelin, and M. Chamarro, Nanoscale **12**, 18978 (2020).

[44] J. Ramade, L. M. Andriambariarijaona, V. Steinmetz, N. Goubet, L. Legrand, T. Barisien, F. Bernardot, C. Testelin, E. Lhuillier, A. Bramati, and M. Chamarro, Nanoscale **10**, 6393 (2018).

[45] P. O. Löwdin, J. Chem. Phys. **19**, 1396 (1951).

[46] L. M. Roth, B. Lax, and S. Zwerdling, Phys. Rev. **114**, 90 (1959).

[47] J. M. Luttinger, Phys. Rev. **102**, 1030 (1956).

[48] M. H. Weiler, R. L. Aggarwal, and B. Lax, Phys. Rev. B **17**, 3269 (1978).

[49] L. R. Ram-Mohan, K. H. Yoo, and R. L. Aggarwal, Phys. Rev. B **38**, 6151 (1988).

[50] M. Plihal and D. L. Mills, Phys. Rev. B **52**, 12813 (1995).

[51] G. F. Koster, J. O. Dimmock, R. G. Wheeler, and H. Statz, *Properties of the Thirty-Two Point Groups* (MIT Press, Cambridge, MA, 1963), Table 35, p. 46.

[52] P. S. Grigoryev, V. V. Belykh, D. R. Yakovlev, E. Lhuillier, and M. Bayer, Nano Lett. **21**, 8481 (2021).

[53] M. J. Crane, L. M. Javoby, T. A. Cohen, Y. Huang, C. K. Luscombe, and D. Gamelin, Nano Lett. **20**, 8626 (2020).

[54] A. Ghribi, R. Ben Aich, K. Boujdaria, T. Barisien, L. Legrand, M. Chamarro, and C. Testelin, Nanomaterials **11**, 3054 (2021).

[55] M. A. Becker, R. Vaxenburg, G. Nedelcu, P. C. Sercel, A. Shabaev, M. J. Mehl, J. G. Michopoulos, S. G. Lambrakos, N. Bernstein, J. L. Lyons, T. Stöferle, R. F. Mahrt, M. V. Kovalenko, D. J. Norris, G. Rainò, and A. L. Efros, Nature (London) **553**, 189 (2018).

[56] Z. Yang, A. Surrente, K. Galkowski, N. Bruyant, D. K. Maude, A. A. Haghighirad, H. J. Snaith, P. Plochocka, and R. J. Nicholas, J. Phys. Chem. Lett. **8**, 1851 (2017).

[57] Z. Yang, A. Surrente, K. Galkowski, A. Miyata, O. Portugall, R. J. Sutton, A. A. Haghighirad, H. J. Snaith, D. K. Maude, P. Plochocka, and R. J. Nicholas, ACS Energy Lett. **2**, 1621 (2017).

[58] Note that a large part of the DFT calculations in the literature has been performed in the cubic or pseudocubic crystal symmetry.

[59] B. Traore, J. Even, L. Pedesseau, M. Kepenekian, and C. Katan, Phys. Rev. Mater. **6**, 014604 (2022).

[60] Y. Su, H. Wang, L.-B. Shi, Y.-Z. Wang, Q. Liu, and P. Qian, Mater. Sci. Semicond. Process. **150**, 106836 (2022).